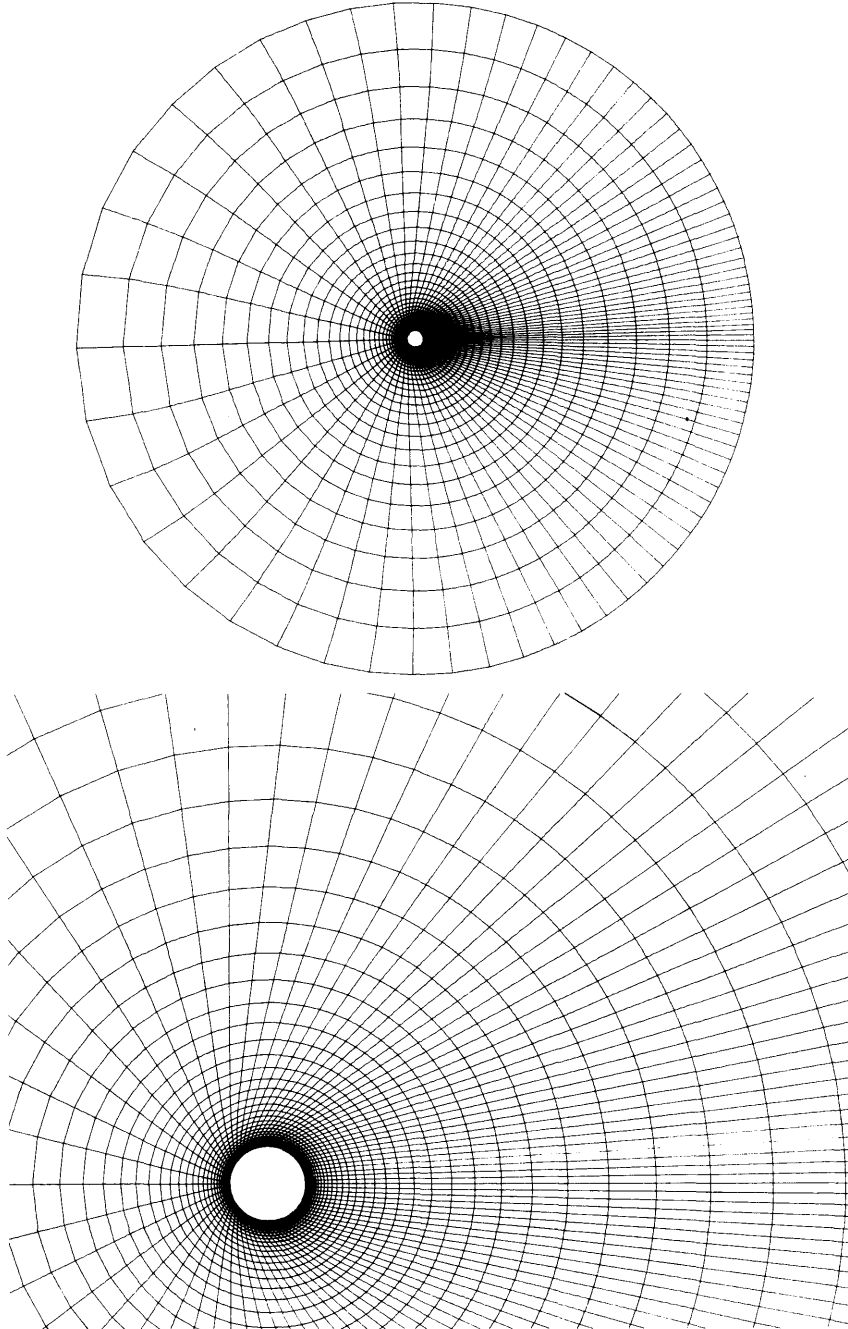


## 8. COMPUTED RESULTS

### (1) Grid

The grid used in the following computations is shown in Fig. 8-1. A direct numerical method 7) was used for the grid generation.



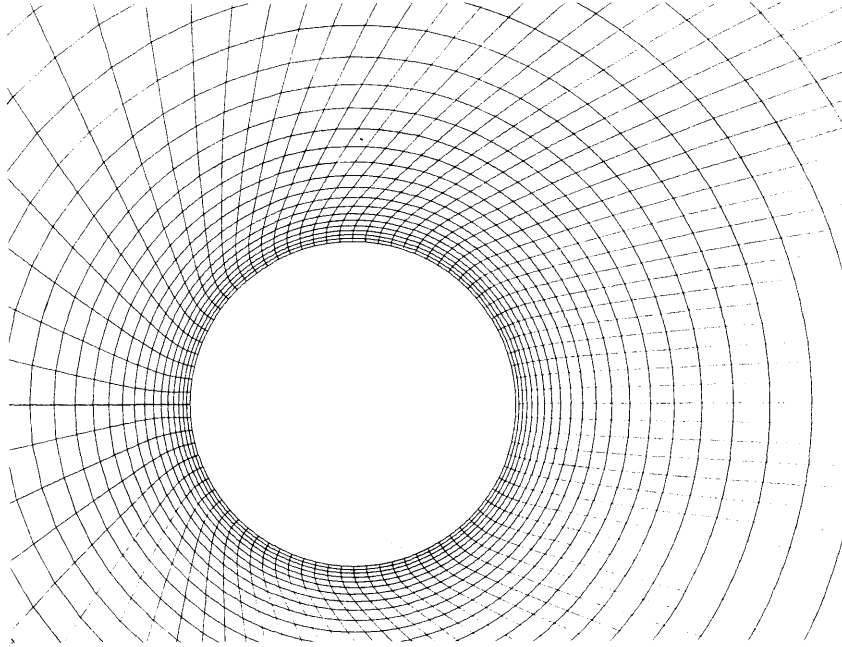


Fig. 8-1 (a)-(c) Grid around a circular cylinder.

A circular cylinder of unit diameter forms an inner boundary. The outer boundary forms a circle whose diameter is 40 times that of the inner circle. The number of grid points are 81 in  $\xi$ -direction and 41 in  $\eta$ -direction. The grids are clustered near solid wall and in the wake region to obtain high resolution there. The minimum  $\eta$ -spacing adjacent to the body is 0.01. 80 points are placed uniformly on the solid wall. A cut along  $\eta$ -axis is placed on the line of symmetry at upstream. It is doubly defined as  $i = 1$  line and  $i = IM$  line. The grid is made orthogonal near solid wall so that the boundary condition for pressure derived in the Appendix may be used.

### (2) Parameters and conditions in computation

The condition shown in Section 7-(4) was used for initial conditions in all the computations shown in the present paper. The boundary conditions used are as shown in Chapter 7.

The parameter  $\theta$  for Padé time differencing shown in eq.(4-1) was set as unity (Euler implicit), and  $\omega_\xi$  and  $\omega_\eta$  for numerical dissipation terms shown in eq.(4-12) were both set as 0.80.

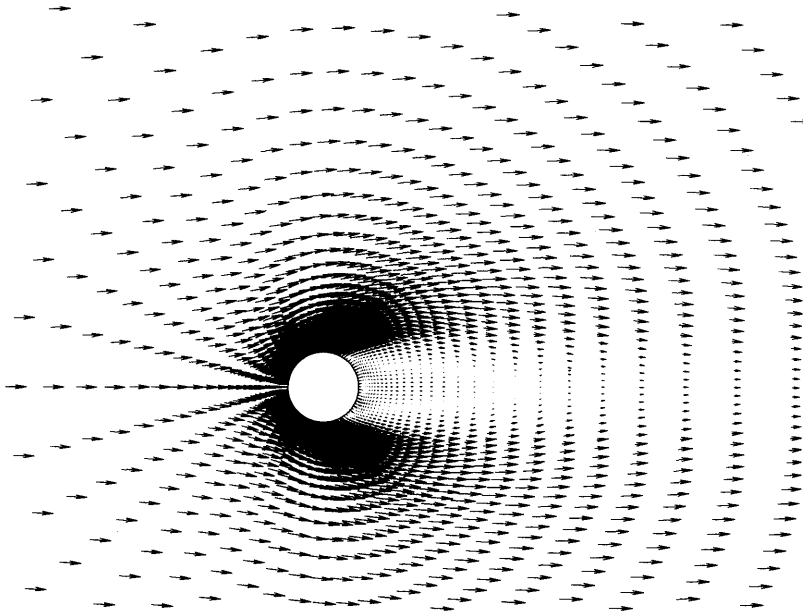
### (3) Convergence criteria

Computation was continued until a convergence parameter reached a certain value. The convergence parameter  $\epsilon_{it}$  is defined as shown below 8).

$$\epsilon_{it} \equiv \frac{\text{Max} \left[ \frac{\text{Max}(\sqrt{(\Delta u)^2 + (\Delta v)^2})}{\text{Max}(\sqrt{u^2 + v^2})}, \frac{\text{Max}(|\Delta p|)}{\text{Max}(p) - \text{Min}(p)} \right]}{\Delta t} \quad (8-1)$$

#### (4) Computed flow fields

Flow velocity vectors at  $Re = 40$  are shown in Fig. 8-2 (a) and (b). The flow is completely symmetric and a twin-vortex is formed aft of the body.



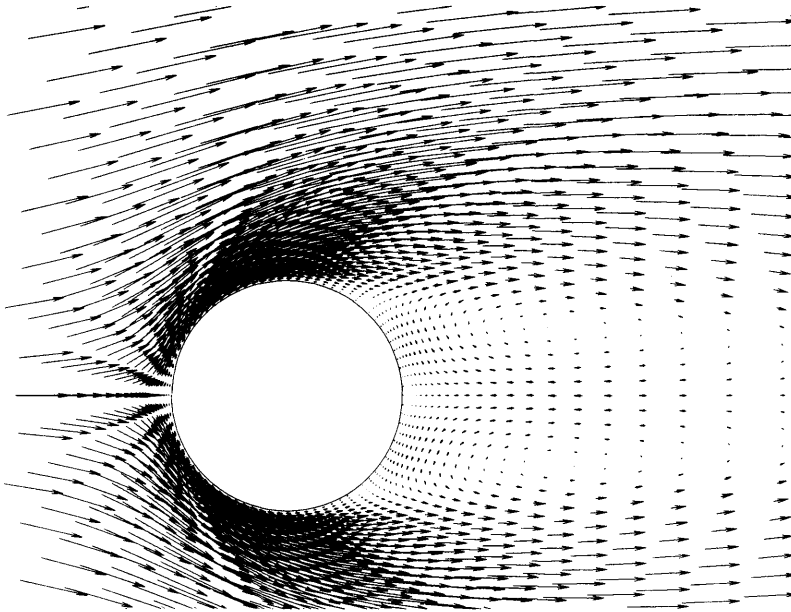
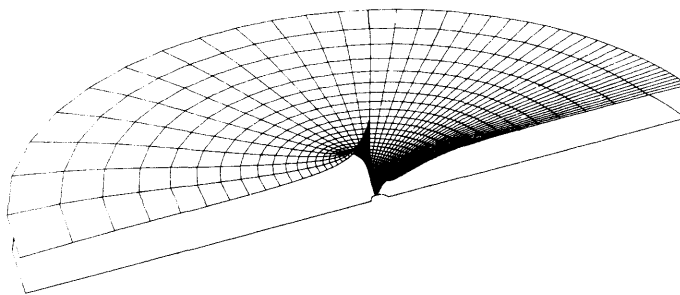


Fig. 8-2 (a), (b) Flow velocity vectors.  $Re = 40$ .

A perspective view of the pressure distribution at  $Re = 40$  is shown in Fig. 8-3 (a) and (b). No oscillation is observed in the distribution, since 4-th order numerical dissipation terms are added to the original equations (see eq. (4-12)).



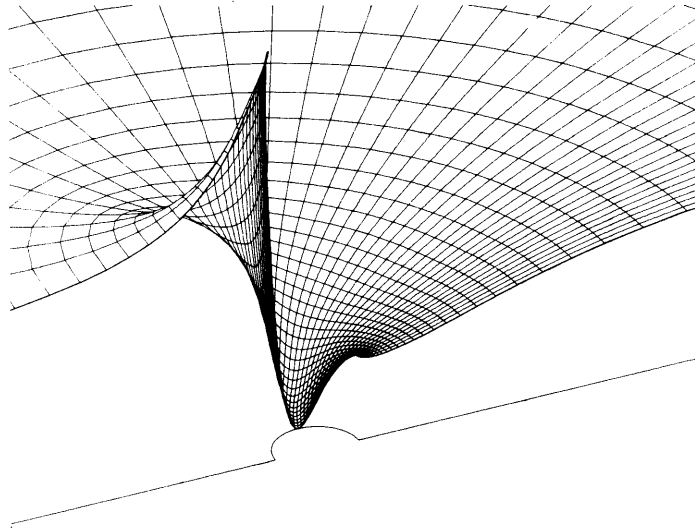


Fig. 8-3 (a), (b) Pressure distribution.  $Re = 40$ .

#### (5) Time history of convergence parameter

The time history of the convergence parameter  $\epsilon_{it}$  at  $Re = 40$  is shown in Fig. 8-4.  $\epsilon_{it}$  is defined in eq.(8-1). It shows exponential decay both in cases  $\Delta t = 0.5$  and  $\Delta t = 1.0$ , though short wave oscillations appear on the curves. At  $\Delta t = 1.0$ ,  $\epsilon_{it}$  reduces to about  $1.0 \times 10^{-6}$  after 200 timesteps. This means that the computed values will change 0.1% at most in the next 1000 timesteps. In a timestep  $\Delta t = 1.0$ , a flow particle travels a distance equal to the diameter of the cylinder with a freestream speed. Therefore, it may be stated that the solution with  $\Delta t = 1.0$  is converged after 200 time-

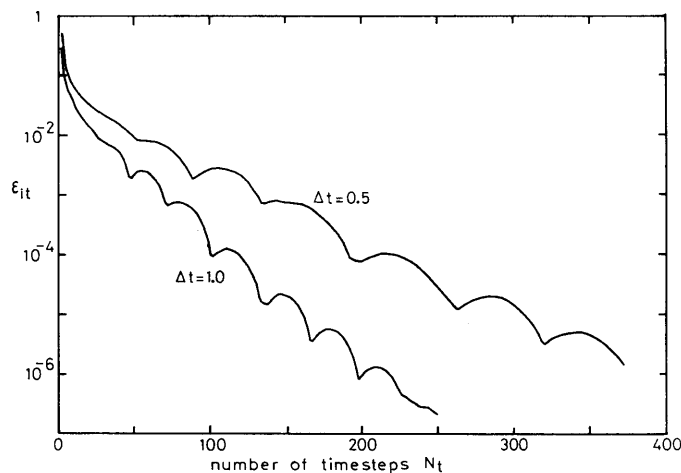


Fig. 8-4 Convergence parameter  $\epsilon_{it}$ .  $Re = 40$ .

steps. The CPU time required per timestep is 25 seconds, using the Fujitsu FACOM M-180IIAD computer at the Ship Research Institute.

The number of timesteps needed for reducing  $\epsilon_{it}$  to a specified value at  $\Delta t = 1.0$  is about half of that at  $\Delta t = 0.5$ . However, the computation at  $\Delta t = 2.0$  showed poorer convergence than  $\Delta t = 1.0$ . Therefore, it may be stated that practically the maximum allowable timestep  $\Delta t$  is about 1.0 in the present computation.

#### (6) Truncation error analysis

The truncation error analysis was made using the method shown in Chapter 6.

Before analyzing the flow field, the accuracy of the method and the computer code was checked, using the grid shown in Fig. 8-1. First, a model function which is linear with  $x$  and  $y$  was used. The results satisfied eqs. (6-35) and (6-37) with an accuracy of more than four significant figures. Second, a model function which is quadratic with  $x$  and  $y$  was used. The second differencings thus obtained agreed with the exact values with an accuracy of approximately three significant figures.

The distribution of the points where the analysis was made is shown in Fig. 8-5. The results are shown in Table 8-1 (a)-(e). The numbers 1 — 7 in the table correspond to those in eqs. (6-29) — (6-31). \* denotes difference, and  $\sim$  denotes truncation error, both of which are estimated using the method described in Chapter 6. The magnitude of the terms representing differences and truncation errors in the table is normalized using the term of

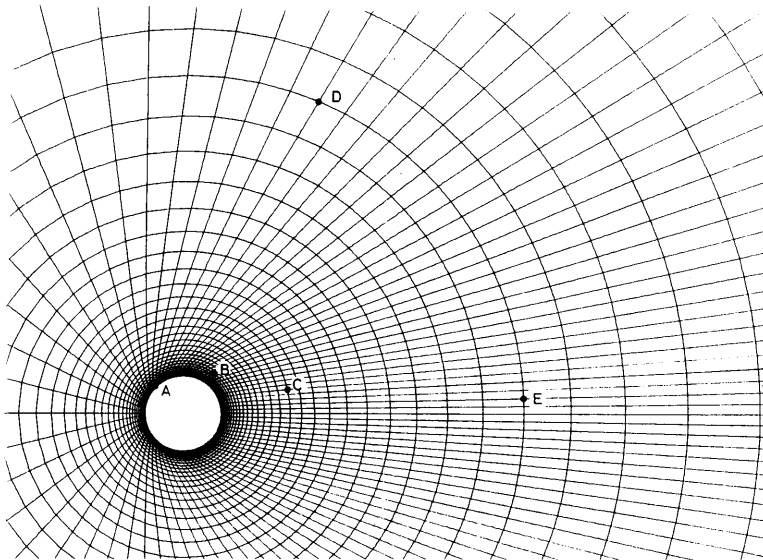


Fig. 8-5 Spatial point distribution for truncation error analysis.

Table 8-1 Truncation error analysis.  $Re = 40$ .

(a) Point A  $i = 15, j = 3$

```

*****
I=15 J=3
X-MOMENTUM EQUATION.
  ①      ②      ③      ④      ⑤      ⑥      ⑦
* -0.510  0.523  -1.00  0.706D-01  0.917  0.102D-04  -0.141D-03
~ -0.267D-02  0.269D-02  0.967D-02  0.138D-02  0.521D-02
  MAX=-1.3205  AT L= 3  SUM=-0.96910D-03
Y-MOMENTUM EQUATION.
  ①      ②      ③      ④      ⑤      ⑥      ⑦
* -0.558  0.456  -0.437  -0.460  1.00  -0.221D-05  -0.193D-03
~ -0.514D-02  0.444D-02  -0.355D-01  -0.710D-02  0.125D-01
  MAX= 0.77077  AT L= 5  SUM= 0.63175D-03
CONTINUITY EQUATION.
  ①      ②      ③      ④      ⑤      ⑥      ⑦
* -1.00  1.00
~ -0.524D-02  0.972D-02
  MAX=-3.6412  AT L= 1  SUM= 0.12530D-03
*****

```

(b) Point B  $i = 28, j = 10$

```

*****
I=28 J=10
X-MOMENTUM EQUATION.
  ①      ②      ③      ④      ⑤      ⑥      ⑦
* 0.539D-01  -0.506D-01  1.00  -0.460D-01  -0.957  -0.100D-03  -0.103D-04
~ 0.917D-03  -0.186D-04  0.372D-02  0.451D-03  -0.384D-02
  MAX= 0.24815  AT L= 3  SUM= 0.86090D-04
Y-MOMENTUM EQUATION.
  ①      ②      ③      ④      ⑤      ⑥      ⑦
* 0.297  0.107D-01  0.675  0.155D-01  -1.00  -0.134D-04  -0.162D-04
~ 0.820D-02  0.374D-03  0.259D-01  0.168D-02  0.515D-03
  MAX=-0.55496D-01 AT L= 5  SUM= 0.87758D-04
CONTINUITY EQUATION.
  ①      ②      ③      ④      ⑤      ⑥      ⑦
* 1.00  -1.00
~ 0.170D-01  -0.351D-01
  MAX=-0.86580D-01 AT L= 2  SUM=-0.46554D-06
*****

```

(c) Point C  $i = 36, j = 20$

```

*****
I=36 J=20
X-MOMENTUM EQUATION.
  ①      ②      ③      ④      ⑤      ⑥      ⑦
* 0.129D-01  -0.948D-01  1.00  -0.198D-01  -0.899  0.406D-04  0.245D-04
~ -0.782D-04  0.163D-04  0.160D-02  -0.137D-03  0.282D-03
  MAX= 0.64025D-01 AT L= 3  SUM=-0.17126D-04
Y-MOMENTUM EQUATION.
  ①      ②      ③      ④      ⑤      ⑥      ⑦
* -0.470  0.192  0.274  -1.00  0.996  0.207D-02  -0.895D-03
~ -0.193D-02  0.952D-03  -0.110  -0.124D-01  0.307D-01
  MAX=-0.17031D-02 AT L= 4  SUM= 0.11277D-04
CONTINUITY EQUATION.
  ①      ②      ③      ④      ⑤      ⑥      ⑦
* 1.00  -1.00
~ -0.609D-02  -0.497D-02
  MAX= 0.38823D-01 AT L= 1  SUM= 0.30767D-05
*****

```

(d) Point D  $i = 15, j = 30$ 

```

*****
I=15 J=30
X-MOMENTUM EQUATION.
  ①      ②      ③      ④      ⑤      ⑥      ⑦
* 1.00    -0.979D-01 -0.905    0.351D-01 -0.311D-01  0.328D-02  0.164D-02
~ -0.311D-01 -0.375D-04  0.133D-01  0.987D-03  0.135D-03
MAX= 0.60946D-02AT L= 1    SUM= 0.34722D-04
Y-MOMENTUM EQUATION.
  ①      ②      ③      ④      ⑤      ⑥      ⑦
* -0.987   -0.128D-01  1.00    0.316D-03 -0.327D-03 -0.736D-04 -0.736D-04
~ -0.339D-02  0.478D-04  0.121D-02 -0.862D-04 -0.294D-04
MAX= 0.16983D-01AT L= 3    SUM= 0.10747D-05
CONTINUITY EQUATION.
  ①      ②      ③      ④      ⑤      ⑥      ⑦
* 0.996     -1.00    0.000    0.000    0.000    -0.171D-04  0.768D-04
~ -0.310D-01  0.373D-02  0.000    0.000    0.000
MAX=-0.58566D-02AT L= 2    SUM= 0.23485D-04
*****

```

(e) Point E  $i = 39, j = 30$ 

```

*****
I=39 J=30
X-MOMENTUM EQUATION.
  ①      ②      ③      ④      ⑤      ⑥      ⑦
* 0.429   -0.157   0.724   0.735D-02 -1.00    -0.926D-03 -0.272D-03
~ 0.400D-02  0.521D-03  0.588D-02  0.134D-03 -0.496D-02
MAX=-0.36732D-01AT L= 5    SUM=-0.57529D-04
Y-MOMENTUM EQUATION.
  ①      ②      ③      ④      ⑤      ⑥      ⑦
* 0.343   1.00    -0.340  -0.105D-01 -0.991   -0.463D-03 -0.163D-02
~ 0.386D-02  0.693D-02  0.146D-01 -0.300D-03  0.345D-02
MAX= 0.13795D-02AT L= 2    SUM=-0.11232D-05
CONTINUITY EQUATION.
  ①      ②      ③      ④      ⑤      ⑥      ⑦
* 1.00     -1.00    0.000    0.000    0.000    -0.632D-06  0.135D-03
~ -0.934D-02 -0.693D-02  0.000    0.000    0.000
MAX=-0.79173D-01AT L= 2    SUM= 0.15206D-04
*****

```

maximum absolute value in each equation, and the maximum absolute value is shown as titled "MAX=". "L=" shows the number of the term used for normalization. "SUM=" denotes [residual] shown in eqs. (6-29) – (6-31). It is the sum of the terms representing differences in the equations. If a steady-state is completely reached, the sum must be zero. The term is not normalized, therefore the ratio SUM/MAX indicates how closely the solution obtained reaches steady-state.

The point A is in the shear layer attached on the solid wall. All the physical terms in the three equations are large.

The point B is in the free shear layer shortly after separation. The x-momentum equation shows that the pressure gradient is balanced by the shear-stress term. Since the direction of the flow is approximately parallel with x-axis, all the terms in the y-momentum equation are small.

The point C is close to the core of the wake bubble. All the terms are small.

The point D is located away from the cylinder and the wake region. The flow is almost irrotational, and all the viscous terms are small.

The point E is in the wake region away from the cylinder. Though all

the terms are small, the viscous terms are relatively large, which is in contrast to the point D.

Finally, considering all the results shown in Table 8-1, it may be stated that:

- a) The present computed results may be considered as the steady-state solution with a good accuracy.
- b) The truncation errors are very small compared with the main differenced terms. Therefore, the current differenced form of equations approximates the true differential equations accurately.
- c) The 4-th order numerical dissipation terms explicitly added to the original equations are so small that the accuracy of the solution is not degraded by them.

### (7) Comparison with experiments

Pressure distribution on the cylinder at  $Re = 40$  is shown in Fig. 8-6, together with the experimental data by Grove et al (9) and Thom (10). The computed values show good agreement with experiments, especially with Grove's results. The reason may be that the Grove's results were obtained under smaller wall effect than Thom's, and that the computation was made under even smaller wall effect. The wall effect parameter  $d/h$  in the figure is such that  $d$  is the diameter of the cylinder and  $h$  is the distance between upper and lower surrounding walls.

Computed pressure distributions on the cylinder at  $Re = 10, 20, 40,$  and  $80$  are shown in Fig. 8-7. All the computations were made using a timestep  $\Delta t = 1.0$ . The computed results are symmetric, and no sign of asymmetry or instability is observed.

The front stagnation pressures are shown in Fig. 8-8. The solid line in

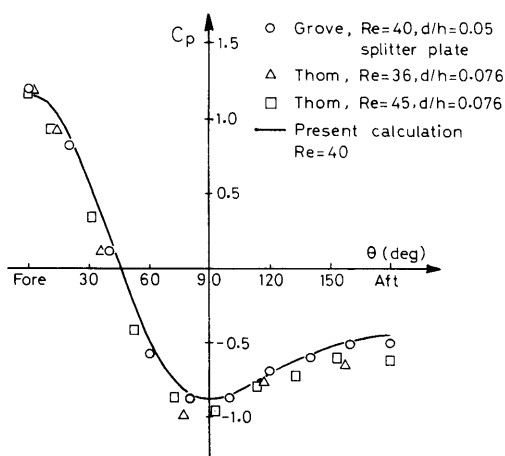


Fig. 8-6 Pressure distribution on a circular cylinder.  $Re = 40$ .

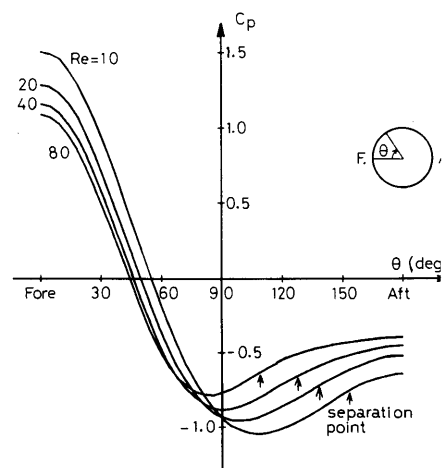


Fig. 8-7 Computed pressure distributions.  $Re = 10, 20, 40$  and  $80$ .

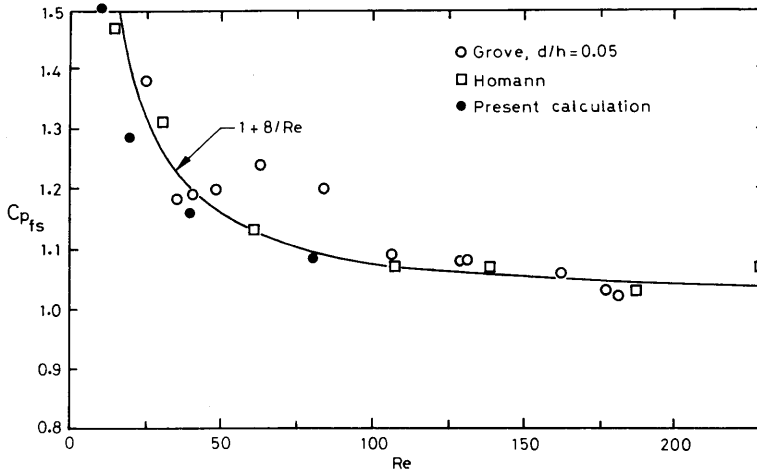


Fig. 8-8 Front stagnation pressure coefficient  $C_{p_{fs}}$ .

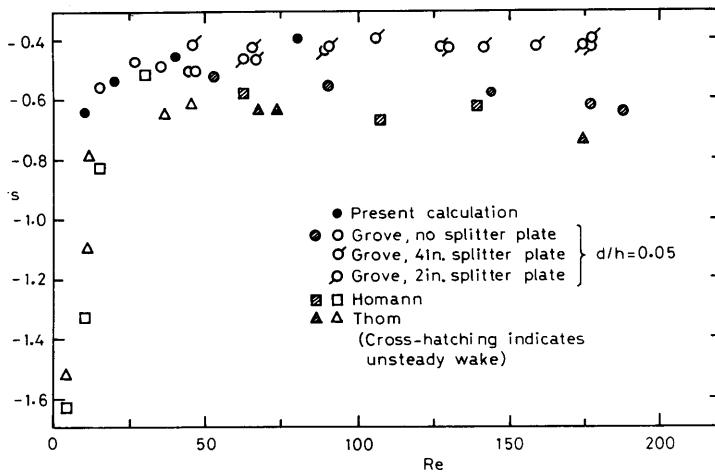


Fig. 8-9 Rear stagnation pressures coefficient  $C_{p_{rs}}$ .

the figure indicates theoretical values derived by Grove 9), using the concept of the boundary layer. The present computations show reasonable agreement with the experiments, and show good agreement with theoretical values by Grove especially at higher Reynolds numbers, where the boundary-layer concept becomes valid.

The rear stagnation pressures are shown in Fig. 8-9. The computed results show good agreement with Grove's results, where a splitter plate was used in order to stabilize the flow and maintain the symmetry of the vortex wake. No such device was needed in the computation, since numerical disturbances are much smaller than those in the real flow.

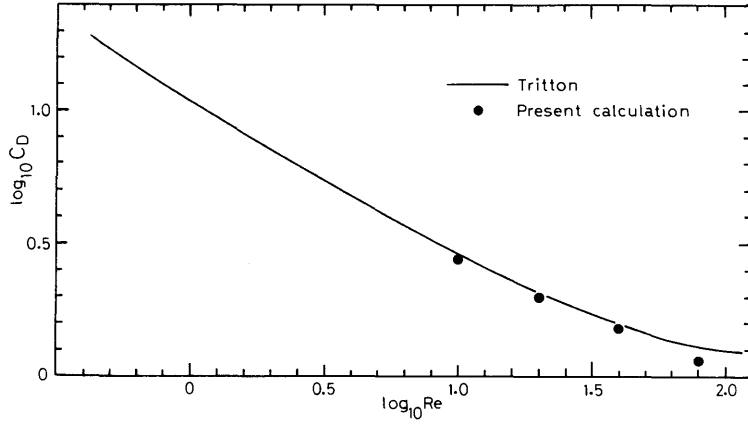


Fig. 8-10 Drag coefficient  $C_D$ .

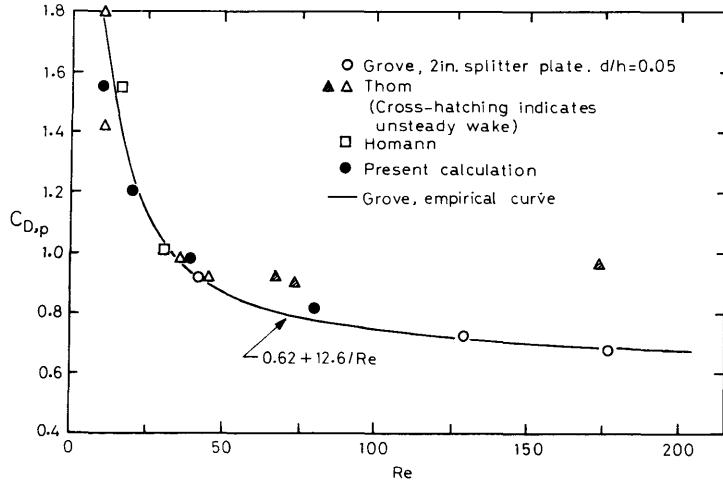


Fig. 8-11 Pressure drag coefficient  $C_{D,p}$ .

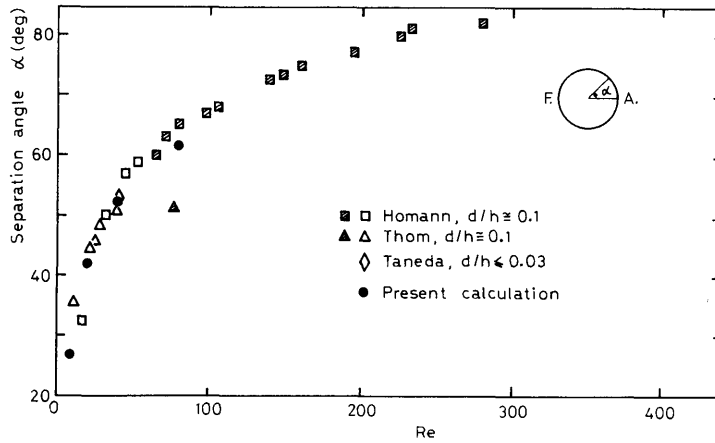


Fig. 8-12 Separation angle.

Drag coefficients are shown in Fig. 8-10. Tritton's experimental curve 11) is shown by a solid line. The computed drag coefficients were obtained using the method described in Appendix A2. They agree well with the experimental curve at  $Re = 10, 20,$  and  $40,$  though the curve is slightly higher. The reason for the deviation at  $Re = 80$  may be that the computed flow is completely symmetric, while oscillations appear in the real flow.

Pressure drag coefficients  $C_{D,p}$  are compared with several experiments in Fig. 8-11. The computation of  $C_{D,p}$  was made by picking up only the contribution by pressure in eq. (A2-6) in Appendix A2. The agreement is again good.

Separation angle  $\alpha$  is shown in Fig. 8-12.  $\alpha$  is defined as an angle from the aft-end point. They show good agreement with experiments.

Wake bubble length  $X_L$  is shown in Fig. 8-13.  $X_L$  is defined as the distance between the wake stagnation point and the cylinder center, following Grove (9). They are in excellent agreement with the experiments by Taneda (13) and Homann (12). The Grove's results do not agree with the other data, which may be due to the wall effect.

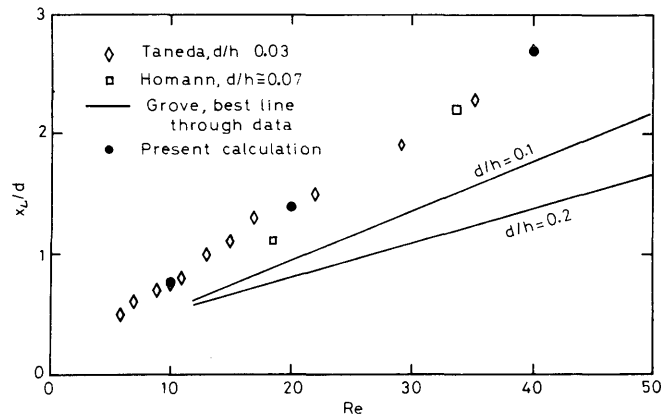


Fig. 8-13 Wake bubble length.

### (8) Results at $Re = 160$

Computation was made at  $Re = 160$ . This time, the steady-state was not reached, and the flow became unstable and unsymmetrical. It is shown in Fig. 8-14. The vortex shedding which is similar to the Karman vortex in the real flow is observed. This shows the potential of the present computational scheme to time-accurate problems, though anything further cannot be stated in the present context.

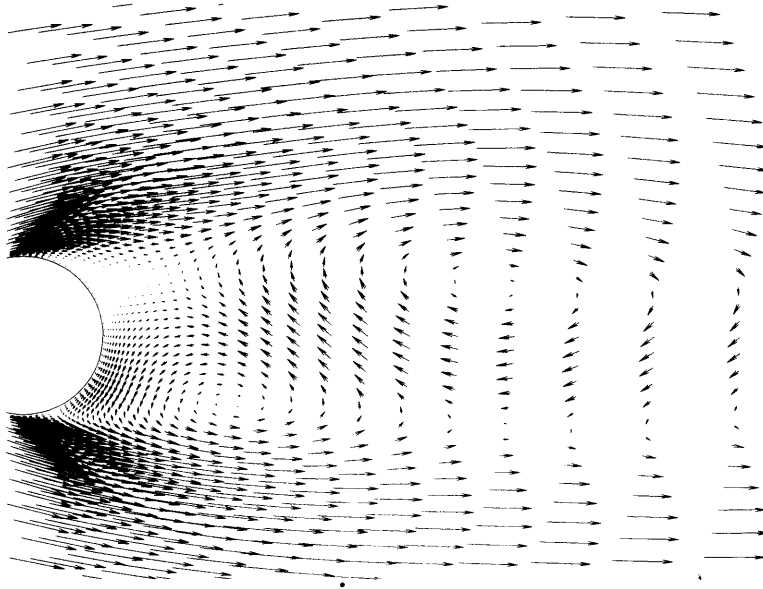


Fig. 8-14 Unsteady vortex shedding at  $Re = 160$ .

## 9. CONCLUSIONS

There are two ways for evaluating a computed result. One is to compare it with experiments. The other is to estimate the magnitude of numerical errors arising at various stages in the computation and to assure that the solution obtained is reliable.

The present work is aimed at fulfilling the latter requirement as much as possible. The truncation error analysis in Chapter 6 together with the computed results demonstrates how accurately the finite difference equations approximate the original differential equations.

The agreement with measurements is very good, in general. It seems to the present author that some of the measurements are affected by the wall effect, which causes discrepancy from the computed results.

The accuracy and efficiency of the present implicit factored method for solving the incompressible Navier-Stokes equations have thus been successfully demonstrated. Future tasks are, the extension to three-dimensional problems, modification to time-accurate scheme, and inclusion of a turbulence model for solving high Reynolds number flows. The extension to three-dimensional flows is straightforward, because the present scheme is written in vector form. The approximate factorization is also valid in three-dimensions. Unsteady flows will be solved using the present scheme, if one uses a simple corrective procedure adopted by Steger et al. 4) for the continuity equation. The easiest way of including a turbulence model is to use

the eddy viscosity model 3). The inclusion of a more complex turbulence model, such as the  $k-\epsilon$  model, is possible, because the added equations for  $k$  and  $\epsilon$  have forms similar to the momentum equations.  $k$  and  $\epsilon$  are simply added to the vector  $q$ .

Therefore it may be stated that the implicit factored method has the potential for solving more complex flows in the future.

## 10. ACKNOWLEDGEMENTS

The main body of the theoretical formulation of the present work was made during the author's stay as a visiting scholar at the Mechanical Engineering Department of the Stanford University from September 1982 to September 1983. The author wishes to thank, first of all, Professor Joel H. Ferziger at the Mechanical Engineering Dept. who guided and assisted the author in many ways for conducting the research during the stay. The author thanks Professor Steven J. Klein of the Mech. Engineering Dept. who gave the author permission to stay at the department. The author also thanks Professor W.C. Reynolds of the department and Dr. Joseph L. Steger at NASA Ames Research Center for valuable discussions in the course of the study. Finally, the author wishes to thank all the CFD guys at the Mechanical Engineering Department of the Stanford University, who made the author's stay there valuable and enjoyable.

The computations were made using the Fujitsu FACOM M-180IIAD computer at the computer center of the Ship Research Institute.

## APPENDIX

### A1 Boundary condition for pressure on solid wall

#### (1) First fundamental quantities of $(\xi, \eta)$ curves (ref. 6)

Mapping of  $(x, y)$  plane to  $(\xi, \eta)$  plane is defined by

$$\begin{cases} \xi = \xi(x, y) \\ \eta = \eta(x, y) \end{cases} \quad \text{or} \quad \begin{cases} x = x(\xi, \eta) \\ y = y(\xi, \eta) \end{cases} \quad (3-1)$$

First fundamental quantities  $E, F,$  and  $G$  are defined as

$$ds^2 = E d\xi^2 + 2F d\xi d\eta + G d\eta^2 \quad (A1-1)$$

where  $ds$ : line element.

$$\begin{cases} E \equiv x_\xi^2 + y_\xi^2 \\ F \equiv x_\xi x_\eta + y_\xi y_\eta \\ G \equiv x_\eta^2 + y_\eta^2 \\ H \equiv \sqrt{EG - F^2} = \frac{1}{J} \end{cases} \quad (A1-2)$$

Line elements  $ds_\xi$  along  $\xi$ -axis and  $ds_\eta$  along  $\eta$ -axis, and an angle  $\omega$  between them are (Fig. A1-1),

$$\begin{cases} ds_\xi = \sqrt{E} d\xi \\ ds_\eta = \sqrt{G} d\eta \\ \cos \omega = \frac{F}{\sqrt{EG}}, \quad \sin \omega = \frac{1}{J\sqrt{EG}} \end{cases} \quad (A1-3)$$

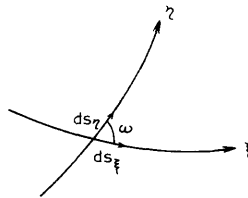


Fig. A1-1 Line elements  $ds_\xi$  and  $ds_\eta$

#### (2) $x$ - and $y$ -momentum equations

Original momentum equations (2-1) and (2-2) are transformed into 1st

and 2nd components of eq. (3-8), using eq. (3-1).

Boundary conditions for  $u$  and  $v$  imposed on solid wall are,

$$u = v = 0 \text{ on solid wall}$$

Using the above condition in the transformed momentum equations (Fig. A1-2),

$$\begin{cases} ap_{\xi} + bp_{\eta} = \frac{1}{Re} (\hat{b}u_{\xi\eta} + \hat{c}u_{\eta\eta} + \hat{e}u_{\eta}) \\ cp_{\xi} + dp_{\eta} = \frac{1}{Re} (\hat{b}v_{\xi\eta} + \hat{c}v_{\eta\eta} + \hat{e}v_{\eta}) \end{cases} \quad (\text{A1-4})$$

### (3) Momentum equation in direction normal to $\xi$ -axis

Using eq. (A1-3),  $\mathbf{e}^{\xi}$ , which is a unit vector along  $\xi$ -axis, is

$$\mathbf{e}^{\xi} = \left( \frac{x_{\xi}}{\sqrt{E}}, \frac{y_{\xi}}{\sqrt{E}} \right) \quad (\text{A1-5})$$

$\mathbf{e}^n$ , a unit vector in direction normal to  $\xi$ -axis, is then,

$$\mathbf{e}^n \equiv (e_x^n, e_y^n) = \left( -\frac{y_{\xi}}{\sqrt{E}}, \frac{x_{\xi}}{\sqrt{E}} \right) \quad (\text{A1-6})$$

The momentum equation in  $\mathbf{e}^n$  direction is obtained as

$$\begin{aligned} [\text{momentum eq. in } \mathbf{e}^n \text{ direction}] &= e_x^n [x\text{-momentum eq.}] \\ &+ e_y^n [y\text{-momentum eq.}] \end{aligned}$$

Therefore,

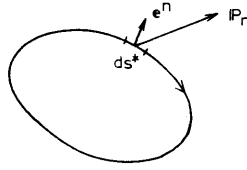
$$\begin{aligned} &-\frac{JF}{\sqrt{E}} p_{\xi} + J\sqrt{E} p_{\eta} \\ &= \frac{1}{Re} \left[ -\frac{y_{\xi}}{\sqrt{E}} (\hat{b}u_{\xi\eta} + \hat{c}u_{\eta\eta} + \hat{e}u_{\eta}) + \frac{x_{\xi}}{\sqrt{E}} (\hat{b}v_{\xi\eta} + \hat{c}v_{\eta\eta} + \hat{e}v_{\eta}) \right] \end{aligned} \quad (\text{A1-7})$$

Let a coordinate  $(m, n)$  be such that  $m$  aligns with  $\xi$  and  $n$  is normal to them, and that both  $m$  and  $n$  have scale of unity (cf. Fig. A1-2). Then,

$$\begin{cases} dm = \sqrt{E} d\xi + \sqrt{G} \cos \omega d\eta \\ dn = \sqrt{G} \sin \omega d\eta \end{cases} \quad (\text{A1-8})$$

$$\begin{cases} \xi_n = -\frac{JF}{\sqrt{E}} \\ \eta_n = J\sqrt{E} \end{cases} \quad (\text{A1-9})$$



Fig. A2-1 Force  $IP_n$  acting on a solid body

, where  $e_x^n$  and  $e_y^n$  are components of a unit normal vector  $e^n$  given in eq. (A1-6) and \* denotes dimensional values.

A total force  $I\mathbf{F}$  is given by integrating  $IP_n$  all along the solid surface.

$$I\mathbf{F} = \begin{bmatrix} Drag \\ Lift \end{bmatrix} = \oint IP_n ds^* \quad (\text{A2-2})$$

By non-dimensionalizing the physical quantities in a way shown in eq. (2-4), the drag and lift coefficients are given as follows.

$$C_D \equiv \frac{Drag}{\frac{1}{2} \rho U_{\infty}^2 L} = 2 \int \left[ e_x^n \left( -p + \frac{2}{Re} \frac{\partial u}{\partial x} \right) + e_y^n \frac{1}{Re} \left( \frac{\partial u}{\partial y} + \frac{\partial v}{\partial x} \right) \right] ds \quad (\text{A2-3})$$

$$C_L \equiv \frac{Lift}{\frac{1}{2} \rho U_{\infty}^2 L} = 2 \int \left[ e_x^n \frac{1}{Re} \left( \frac{\partial u}{\partial y} + \frac{\partial v}{\partial x} \right) + e_y^n \left( -p + \frac{2}{Re} \frac{\partial v}{\partial y} \right) \right] ds \quad (\text{A2-4})$$

The components of vector  $e^n$  are given by

$$e_x^n = -\frac{y_{\xi}}{\sqrt{x_{\xi}^2 + y_{\xi}^2}}, \quad e_y^n = \frac{x_{\xi}}{\sqrt{x_{\xi}^2 + y_{\xi}^2}} \quad (\text{A1-5})$$

In order to integrate in the computational plane,  $x$  and  $y$  derivatives are replaced by  $\xi$ - and  $\eta$ -derivatives. That is,

$$\partial_x = a \partial_{\xi} + b \partial_{\eta}, \quad \partial_y = c \partial_{\xi} + d \partial_{\eta} \quad (\text{A3-4})$$

Since  $\xi$ -axis aligns with the solid body surface, the line element  $ds$  on the solid surface is equal to  $dS_{\xi}$  given in eq. (A1-3).

$$ds = \sqrt{x_{\xi}^2 + y_{\xi}^2} d\xi \quad (\text{A2-5})$$

Using the solid wall boundary condition  $u = v = u_{\xi} = v_{\xi} = 0$ , and substituting eqs. (A1-5), (3-4), and (A2-5) into eqs. (A2-3) and (A2-4),

$$C_D = 2 \int \left[ p y_{\xi} + \frac{J}{Re} \left\{ (x_{\xi}^2 + 2y_{\xi}^2) u_{\eta} - x_{\xi} y_{\xi} v_{\eta} \right\} \right] d\xi \quad (\text{A2-6})$$

$$C_L = 2 \int \left[ -p x_{\xi} + \frac{J}{Re} \left\{ -x_{\xi} y_{\xi} u_{\eta} + (2x_{\xi}^2 + y_{\xi}^2) v_{\eta} \right\} \right] d\xi \quad (\text{A2-7})$$

### REFERENCES

- 1) Beam, R.M. and Warming, R.F.; "An Implicit Factored Scheme for the Compressible Navier-Stokes Equations." AIAA Journal Vol. 16, No. 4, April 1978.
- 2) Warming, R.F. and Beam, R.M.; "On the Construction and Application of Implicit Factored Schemes for Conservation Laws." SIAM-AMS Proceedings vol. 11, 1978, pp. 85-129.
- 3) Steger, J.L.; "Implicit Finite difference Simulation of Flow about Arbitrary Two-dimensional Geometries", AIAA Journal vol. 16, No. 7, July 1978. pp. 679-686.
- 4) Steger, J.L. and Kutler, P.; "Implicit Finite Difference Procedures for the Computation of Vortex Wakes," AIAA Journal vol. 15, No. 4, April 1977. pp. 581-590.
- 5) Beam, R.M. and Warming, R.F.; "Alternating Direction Implicit Methods for Parabolic Equations with a Mixed Derivative," NASA Technical Memorandum 78569. March 1979.
- 6) Terazawa, K.; "Shizenkagakusha no Tame no Suugaku Gairon (Zooteiban)," Iwanami Shoten 1973.
- 7) Kodama, Y.; "A Direct Numerical Control Method for Grid Generation," Proceedings of the 3rd NAL Symposium on Aircraft Computational Aerodynamics. NAL June 1985 (To be published).
- 8) Kodama, Y.; "Computation of the Two-Dimensional Incompressible Navier-Stokes Equations Using an Implicit Factored Method," Proceeding of the 2nd NAL Symposium on Aircraft Computational Aerodynamics. NAL SP-3, 1984.
- 9) Grove, A.S., Shair, E.S., Petersen, E.E., and Acrivos, A.; "An experimental investigation of the steady separated flow past a circular cylinder," JFM vol. 19, 1964. pp. 60-80.
- 10) Thom, A.; "The flow past circular cylinders at low speeds," Proc. Roy. Soc. A, vol. 141, 1933. p651.
- 11) Tritton, D.J.; "Experiments on the flow past a circular cylinder at low Reynolds numbers," JFM vol. 6, 1959. pp. 547-567.
- 12) Homann, F.; "Einfluss grösser Zähigkeit bei Strömung um Zylinder," Fösch. IngWes. 7. 1936. p1.
- 13) Taneda, S.; "Experimental investigation of the wakes behind cylinders and plates at low Reynolds numbers," J. Phys. Soc. Japan, 11, 1956. p302.
- 14) Chang, J.L.C. and Kwak, D.; "On the Method of Pseudo Compressibility for Numerically Solving Incompressible Flows," AIAA paper AIAA-84-0252, 1984.
- 15) Kwak, D. et al.; "An Incompressible Navier-Stokes Flow Solver in Three-Dimensional Curvilinear Coordinate System Using Primitive Variables," AIAA paper AIAA-84-0253, 1984.
- 16) Smith, G.D.; "Numerical Solution of Partial Differential Equations: Finite Difference Methods", Second Edition. Oxford University Press 1978.